Series-DC Connection of Offshore Wind Generating Units - Modeling, Control and Galvanic Isolation

A. O. Almeida, I. F. Lopes, P. M. Almeida, M. A. Tomim, J. A. Passos Filho, P. G. Barbosa

***Abstract*—This work proposes an air-core DC-DC solid state transformer to connect the wind turbines of an offshore wind farm in series with a DC transmission link. This emerging layout does not use a power transformer to increase the voltage from the offshore collector network to the transmission level, nor does it require a rectifier station to convert the electrical energy to DC. The diode-clamped rectifiers, connected to each permanent-magnet generator, are controlled to drain sinusoidal currents from the generators in order to extract the maximum power from the wind turbines. The air-core transformer, designed by means of a finite element software, ensures the galvanic isolation between the wind generator and the HVDC link. From the generator side, a single-phase full-bridge three-level inverter feeds the primary coil of the transformer, whereas the secondary coil is wound using by means of an XLPE-insulated cable. This paper also presents a strategy for designing the controllers that regulate the output voltage of each wind conversion unit. Results from digital simulations, obtained with PSCAD/EMTDC, are presented to validate the technical feasibility of the proposed DC-DC solid-state transformer scheme, as well as to demonstrate its performance under different operational conditions.**

***Keywords*—Solid-State Transformer, Air-Core Transformer, Series WEC Connection, Offshore Wind Farm.**

I. Introduction

OFFSHORE wind farms have been seen as the economically and logistically viable option for hosting large modern wind turbines (WT) [1]. In addition to the different types and configurations of generators, power electronics converters and harmonic filters [2], the design of the collection network is of fundamental importance to ensure the efficiency and reliability of the wind farm. The collection network connects all generators in parallel to one or two offshore substations, where bulky transformers step up the voltage to the transmission level before exporting the converted energy by means of high voltage alternating current (HVAC) or direct current (HVDC) [3, 4].

Although HVAC transmission systems are widely used to connect wind farms close to the coast, HVDC transmission turns ou to be the best option, when the wind farm site is located far from the coast [5]. Under the HVDC transmission class, two different converter technologies are presently available: (*i*) the line-commutated current converters (LCC), based on thyristors, or (*ii*) the voltage source converters (VSC), based on the self-commutated switches.

The LCC-HVDC system usually requires heavy and bulky Y–Y and Y–Δ transformers and high-power harmonic filters, as well as large smoothing reactors connected to the AC and DC terminals of both rectifier and inverter. The LCC-HVDC systems also require start-up generators, in order to provide the commutation voltage for the valves, synchronous condensers or capacitor banks, to support converters reactive power demand. This additional set of equipment incurs in a significant increase in the size, weight and, ultimately, the cost of offshore substations [6].

A. O. Almeida is with Federal Centre of Technological Education of Minas Gerais, Nepomuceno, MG 37.250-000 Brazil (e-mail of corresponding author: andrei.almeida@engenharia.ufjf.br). I. F. Lopes, P. M. Almeida, M. A. Tomim, J. A. Passos Filho and P. G. Barbosa are with Federal University of Juiz de Fora, Juiz de Fora, MG 36.036-900 Brazil.

Paper submitted to the International Conference on Power Systems Transients (IPST2021) in Belo Horizonte, Brazil June 6-10, 2021.

Thus, to overcome some disadvantages of the LCC-HVDC system, the DC transmission system based on voltage source converters (VSC), or simply VSC-HVDC system, was proposed. The development of high-voltage IGBTs (Insulated Gate Bipolar Transistors) made possible the design of high-power VSCs, which are the basis of modern multilevel VSC-based converters. A multilevel VSC converter, for instance, does not require complex transformers or sophisticated magnetic interfacing structures in order to be connected to the power grid. Furthermore, such converters are also capable of synthesizing output voltages and currents with very low harmonic content, while controlling active and reactive powers independently at the converter, using the nearest-level control (NLC) strategy [7]. The aforementioned features simplify the design of harmonic filters and eliminate the need for reactive power support. Regardless of the converters technology, however, all wind energy conversion (WEC) units are still connected in parallel through an AC medium voltage network to an offshore substation, where the voltage is increased to the transmission level and later converted to DC [1, 3, 4].

From another perspective, Fig. 1 shows an emerging configuration for integration of offshore wind farms, where WEC units are connected in series through the DC terminals of their interfacing rectifiers [4, 5]. This configuration can be expanded to include new generation units and, since it uses neither a power transformer to step-up the offshore voltage to the transmission level nor a rectifier station to convert the generated electricity to DC. Therefore, its efficiency is expected to greater than from other alternatives commonly proposed in the literature. On the other side of the DC link, a modular multilevel converter (MMC) processes the electricity exported by the submarine cables into the onshore power grid.

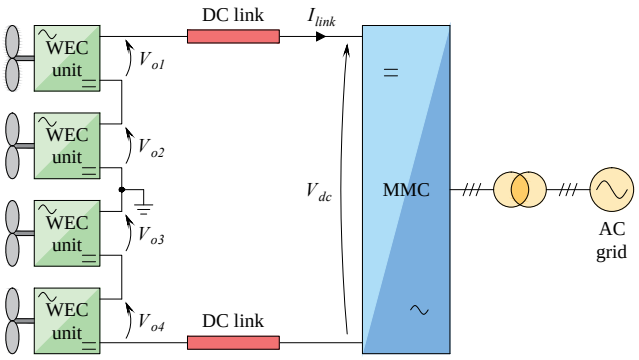

Fig. 1. Wind farm configuration with the WEC units connected in series through their the DC output terminals.

Despite the advantages pointed out, the series configuration imposes some real operational challenges. One, for example, is related to the differences in wind speeds impacting each turbine of the farm. Moreover, the operation of the wind farm must account for situations when the system may undergo the loss of one or more generating units. Another issue that has to be normally tackled in a series layout, as shown in Fig. 1, is associated the galvanic isolation between the WEC components and the DC link. The use of

a three-phase transformer connected to the generator terminals may not be a practical solution due to the frequency of the supply [8], which varies with the generator speed.

Veilleux and Lehn [9] used a low-frequency three-phase transformer to isolate the wind generator from a full-bridge diode rectifier with a buck DC-DC converter, connected in series with the DC link. Despite controlling the generating units with only one self-commutated switch, this type of converter drains rectangular currents from the wind generator, increasing losses and producing pulsating torques on the permanent magnet synchronous generators (PMSG) shafts. Besides the low frequency of the generator, the high harmonic content of the supplied rectangular currents requires the transformer to be overrated. On the other side of the DC link, a thyristor-based line-commutated inverter (LCI) controls the DC link current instead of voltage.

Almeida et al. [10] also use a three-phase transformer to isolate the wind generator from the HVDC link potential. However, the greater number of poles of the PMSG allows the transformer to be excited with higher frequencies. A three-level neutral-point clamped (NPC) rectifiers is controlled to drain sinusoidal currents from PMSG to avoid pulsating torques, while a modular multilevel converter, located in the onshore substation, regulates the current through the HVDC line. As advantages of the chosen MMC topology one can pinpoint the little demand for reactive power compensation or filters, due to the self-commutated switches employed in its structure, at same time it does not suffer with commutation failures even when connected to weak networks.

Unlike previous works, Lundberg [11] connects an isolated DC-DC converter to the output terminals of the WEC rectifiers. The DC-DC converter has an inner-stage where a high-frequency transformer isolates the generator and WEC electrical components from the DC link. The offshore rectifier regulate the power extracted from each wind turbine while the onshore inverter regulates the DC link voltage. Thus, any reduction in the power supplied by one or a group of WEC units will decrease the power supplied by the farm, forcing a decrement in the DC link current. In this manner, the remained WEC rectifiers tend to increase their output voltages to compensate for the DC link voltage. In this condition the DC bus voltages of the rectifiers should be limited to avoid the over-voltage on the DC-DC converter terminals.

Shi et al. [12] also employed a DC-DC converter with a high-frequency transformer connected to the output terminals of the WEC rectifiers. In the proposed configuration, the speed of the wind turbine is controlled in order to store the excess energy in the turbine rotor, preventing the over-voltage in the rectifier output terminals. Variations in turbine velocity, however, cause higher mechanical stresses. Furthermore, other strategies to overcome the over-voltage issue have been proposed in [13] and [14], both integrating a high-frequency transformer in WEC structure.

The first part of this work presents the mathematical modelling of the modular wind generator proposed here for offshore HVDC connection. The control strategies and designs of the compensators used to regulate the currents drained from the PMSG by NPC-rectifier and to control the DC-DC SST supply voltage by the full-bridge converter are presented. The details of the design of the air-core transformer used to isolate the PMSG from the potential of the HVDC link are presented in the second part of this work. An optimization routine is used to minimize the inductances of the air-core transformer in order to maximize the coupling factor and minimize the number of turns of the primary and secondary coils. Then, the design of air core transformer is carried out with the aid of the FEMM software. Finally, simulation results of the system modelled in the PSCAD/EMTDC software will be presented to validated the effectiveness of proposed topology. The results of digital simulations will be used to validate the design of the controllers of the modular wind generator for offshore HVDC series-connection the performance of air-core transformer fed by the full-bridge converter.

II. The Modular Wind Generator for Offshore HVDC Systems

In order to further investigate the operation of the proposed modular generator for offshore HVDC systems, the schematic diagram of the interface converter used for series-DC collection is shown in Fig. 2. In this scheme, each unit is composed by a wind turbine, a direct-drive PMSG connected to a three-level NPC converter and a DC-DC solid state transformer. The solid state transformer, in turn, is composed by a two-leg full-bridge NPC converter connected to the primary coil of a step-up transformer whose output voltage is further processed by a single-phase full-bridge diode rectifier with a capacitor attached to its terminals.

In the next sections more detailed explanations on the adopted control strategies of the whole system will be set forth.

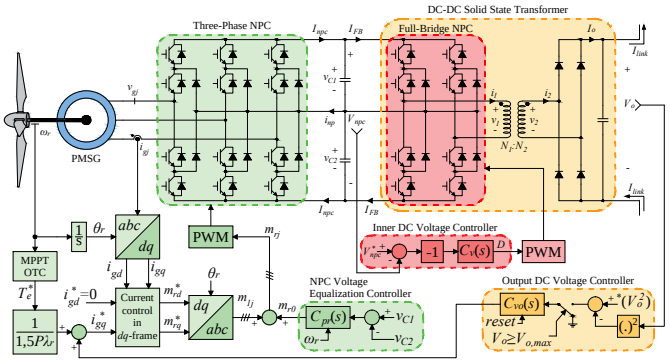

Fig. 2. Schematic diagram of the modular wind generator with DC-DC solid-state transformer.

A. Modelling and control of the PMSG NPC-rectifier

Assuming the PMSG under a balanced operating condition and neglecting any switching harmonics that may be generated by the NPC rectifier, equations (1) and (2) govern the dynamics of the PMSG in *dq* reference frame [15], where R_g, L_{gd} and L_{gq} represent constant equivalent resistances and inductances of generator and its interface filter; v_{rd} and v_{rq} correspond to stator voltages and, therefore, to the voltages at the NPC rectifier terminals; i_{gd} and i_{gq} are the currents drained from the PMSG; ω_r is the angular frequency of the rotor and, finally, λ_r corresponds to the flux produced by permanent magnets. The sub-indexes d and q indicate the variables and quantities referred to the *direct* and *quadrature* axes, respectively.

$$v_{rd} = -R_g\, i_{gd} + \omega_r\, L_{gq}\, i_{gq} - L_{gd}\frac{di_{gd}}{dt} \tag{1}$$

$$v_{rq} = -R_g\, i_{gq} - \omega_r\, L_{gd}\, i_{gd} - L_{gq}\frac{di_{gq}}{dt} + \omega_r\, \lambda_r \tag{2}$$

Considering equal voltages on the DC-side capacitors and the stator voltages proportional to *dq* NPC modulation indexes (m_{rd} and m_{rq}), v_{rd} and v_{rq} can be made $m_{rd}(V_{npc}/2)$ and $m_{rq}(V_{npc}/2)$, respectively, enabling one to write the control relationships (3) and (4) below, where u_d and u_q are control variables for the NPC rectifier.

$$m_{rd} = \left(\frac{2}{V_{npc}}\right)(-u_d + \omega_r\, L_{gq} i_{gq}) \tag{3}$$

$$m_{rq} = \left(\frac{2}{V_{npc}}\right)(-u_q - \omega_r\, L_{gd} i_{gd} + \omega_r \lambda_r) \tag{4}$$

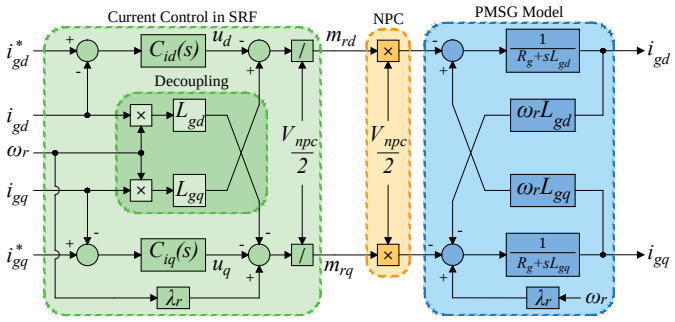

Fig. 3. Control block diagram of the PMSG currents in the *dq*-reference frame.

Applying the Laplace transform to equations (1) to (4), allows one to draw the control block diagram depicted in Fig. 3, in the synchronous reference frame (SRF). A product of this strategy is that the control of the stator currents, i_{gd} and i_{gq}, can now be considered decoupled.

Considering, then, that the PMSG *dq* currents are fully decoupled and compensated, proportional-integral (PI) controllers can be designed to regulate such currents. The open-loop transfer functions for this type of controller can be generalized with the aid of (5), where $k_{p,npc}$ and $k_{i,npc}$ are the proportional and integral gains of the NPC current controllers, respectively, with $m \in [d, q]$.

$$G_{o,m}(s) = \frac{k_{p,npc}}{sL_{gm}} \frac{\left(s + \frac{k_{i,npc}}{k_{p,npc}}\right)}{\left(s + \frac{R_g}{L_{gm}}\right)} \tag{5}$$

Since the real pole of (5) is very close to the imaginary axis of the complex plane, the compensated system will present a slow dynamic response. Thus, canceling the pole of plant with the zero of the PI-controller, results the closed-loop transfer function (6) for the PMSG currents.

$$\frac{I_{gm}(s)}{I^*_{gm}(s)} = \frac{1}{1 + s\tau_{npc}} \tag{6}$$

For a perfect zero-pole cancellation, the proportional and integral gains are given by (7). According to [16], the time constant τ_{npc} can be set between 0.5 and 5 ms in order to ensure a good dynamic response for the NPC rectifier *dq*-currents loops.

$$k_{p,npc} = \frac{L_{gk}}{\tau_{npc}} \qquad k_{i,npc} = \frac{R_g}{\tau_{npc}} \tag{7}$$

Finally, the maximum power of WT can be tracked with an optimal torque control (OTC) algorithm that uses the speed ω_m to compute the reference torque $T^*_m = k_{opt}\omega^2_m$ for the PMSG [15, 17]. The gain k_{opt} depends on the rated parameters of the turbine and be calculated by:

$$k_{opt} = \left(\frac{\rho A C_{p,max}}{22.4 P_b}\right)\left(\frac{\lambda_{opt}\omega_{mb}}{N_{gb}}\right)^3 \tag{8}$$

where $C_{p,max}$ is the maximum coefficient of power, λ_{opt} is the optimal tip speed ratio for the turbine, N_{gb} is the gear ratio of the gearbox and $\omega_m = \omega_{mb}\omega_{pu}$.

Then, setting the *d*–axis current to zero, the reference torque T^*_m can be used to calculate the reference *q*–axis current to drain the maximum power of PMSG.

B. Neutral-point Voltage Balancing of NPC Rectifier

An additional outer control loop must be included in order to equalize voltages v_{C1} and v_{C2} of the NPC DC capacitors, avoiding a circulating current i_{np} [18], which is given by

$$i_{np} = C\frac{d}{dt}\left(v_{C1} - v_{C2}\right) \tag{9}$$

A non-ideal Proportional-Resonant controller, given in (10), can be used to balance the neutral-point voltage and mitigate the third-harmonic voltage ripple [10].

$$C_{pr}(s) = k_{p,res} + k_{r,res}\left(\frac{\omega_b s}{s^2 + \omega_b s + \omega_c^2}\right), \tag{10}$$

where, $k_{p,res}$ and $k_{r,res}$ are the proportional and resonant gains, respectively. Whereas ω_b and ω_c are the bandwidth and the resonance frequency of the non-ideal resonant controller, respectively. Since the generator frequency depends on the wind turbine speed, ω_c must be dynamically adjusted to track ω_r. As for ω_b, literature suggests values between 10 and 30 rad/s [19].

According to Fig. 2 the controller takes the difference between the capacitors' voltages, generating an output signal m_{r0} which is added to PWM modulation indexes m_{rd} and m_{rq} after the *dq-abc* coordinate transformation.

C. Modelling and Control of DC-DC Solid-State Transformer

The DC-DC solid-state transformer (SST), depicted on the right side of Fig. 2, provides galvanic isolation between the wind generator and the HVDC link. The primary coil of the transformer is fed by a full-bridge inverter consisting of a two-arms NPC, while the secondary coil supplies a full-bridge diode rectifier with a DC capacitor connected to its terminals.

The DC-DC SST controller regulates the total DC bus voltage of the NPC rectifier. Thus, when the DC bus voltage increases as a result of the increase in the power amount converted by PMSG, the controller changes its switching pattern to transfer this energy to the HVDC link. Then, according to [8], the following voltage equations can be written:

$$v_1 = R_1 i_1 + L_1\frac{di_1}{dt} - M\frac{di_2}{dt} \tag{11}$$

$$v_2 = -R_2 i_2 + M\frac{di_1}{dt} - L_2\frac{di_2}{dt} \tag{12}$$

where the subindexes $(_1)$ and $(_2)$ refer to the primary and secondary coils, respectively; R_1 and R_2 are the resistances; $L_1 = (L_{\ell 1} + L_{m1})$ and $L_2 = (L_{\ell 2} + L_{m2})$ are the self-inductances; $L_{\ell 1}$ and $L_{\ell 2}$ are the leakage inductances; L_{m1} and L_{m2} are the magnetizing inductances; $M = (L_{m1}/a) = (aL_{m2})$ is the mutual inductance; v_1 and v_2 are the terminal voltages; i_1 and i_2 are the winding currents; and $a = (N_1/N_2)$ is the turns-ratio.

The solution of (11) and (12), disregarding the winding losses, returns the following relation between v_1 and v_2, and di_1/dt:

$$\frac{di_1}{dt} = \frac{L_2 v_1 - M v_2}{L_1 L_2 - M^2} \tag{13}$$

Fig. 4 (a) shows the triangular carriers and the reference signals used to control the switching pattern of the full-bridge inverter. The comparison of the upper and lower carriers with the signals D and $-D$, respectively, generates the modulated width voltage waveform. Fig. 4 (b) shows the idealized waveforms of the voltages at the primary and secondary coils of the transformer. During the interval $t_\alpha \leq t < (T - t_\alpha)$, the single-pulse PWM voltage is $v_1 = +V_{npc}$ and the currents i_1 and i_2 increases from zero to their maximum values, respectively. Throughout this period, as the output rectifier diodes are forward biased, the secondary voltage v_2 will be equal to the DC output voltage V_o. After that period, when v_1 is set to zero, the currents i_1 and i_2 decrease from their maximum values to zero. Fig. 4 (c) shows the idealized waveforms of the currents flowing through the primary and secondary windings of the transformer. Note that the output voltage v_2 is held at V_o even after v_1 goes to zero (Fig. 4 (b)). This behaviour is due to the fact that the current i_2 keeps the output rectifier conducting until all the energy stored in the

transformer is transferred to the output DC capacitor, which happens in $t = t_\beta$. The last plot of Fig. 4 shows the waveform of the real power supplied to the primary winding. All of these steps are repeated when the output voltage is negative, that is, in the negative semi-cycle. However, in this case, the primary and secondary currents decrease from zero to their minimum values when $v_1 = -V_{npc}$ and then, they increase to zero when the voltage $v_1 = 0$.

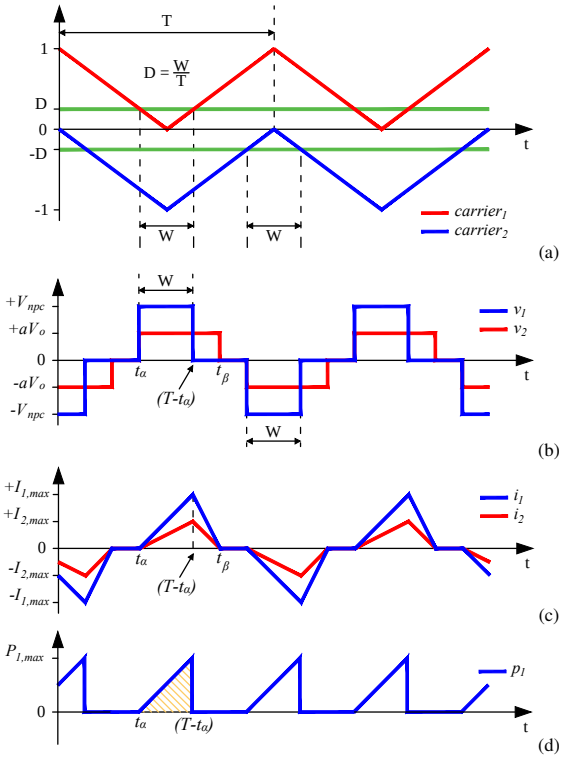

Fig. 4. DC-DC SST waveforms: (a) triangular carriers and control signals; (b) voltages in primary and secondary coils; (c) currents through primary and secondary coils and (d) instantaneous power at primary coil.

The solution of (13) for $v_1 = +V_{npc}$, $v_2 = V_o$, and considering $t_\alpha \leq t < (T - t_\alpha)$ yields:

$$i_1 = m_r(t - t_\alpha) \tag{14}$$

and the solution for $v_1 = 0$, $v_2 = V_o$, and $(T - t_\alpha) \leq t < t_\beta$ returns:

$$i_1 = I_{1,max} + m_f\left(t - T + t_\alpha\right), \tag{15}$$

where $I_{1,max}$ is maximum value of the current i_1 and, m_r and m_f are the rise and fall rates of the primary current, which are calculated respectively by:

$$m_r = \left(\frac{L_2 V_{npc} - M V_o}{L_1 L_2 - M^2}\right) \tag{16}$$

and,

$$m_f = -\left(\frac{M V_o}{L_1 L_2 - M^2}\right) \tag{17}$$

Substituting $t = (T - t_\alpha)$ into (14), the value of $I_{1,max}$ is given by:

$$I_{1,max} = m_r(T - 2t_\alpha) \tag{18}$$

From (15) and (18), it is possible to calculate the instant t_β where the current i_2 reaches zero as follows,

$$t_\beta = \left[1 - \frac{m_r}{m_f}\right](T - 2t_\alpha) + t_\alpha \tag{19}$$

The switching pattern shown in Fig. 4 requires that the difference $(t_\beta - t_\alpha)$ is less than half of the switching period $(T/2)$ to ensure that the voltage v_1 presents a half-wave symmetry. Therefore, based on (16), (17), (19) and considering $(t_\beta - t_\alpha) = T/2$, the following result can be obtained:

$$D_{critical} = \frac{1}{2}\left(\frac{m_f}{m_f - m_r}\right) = \frac{1}{2}\left(\frac{M V_o}{L_2 V_{npc}}\right) \tag{20}$$

where $D = (T - 2t_\alpha)/T$ is the duty-cycle and T is the switching period of the full-bridge inverter.

The value of D calculated in (20) represents the critical value of the duty-cycle that ensures that i_1 and i_2 are not null before the start of negative semi-cycle. In the implementation of the DC-DC SST controller the value of D must be limited between 0 and 0.5. However, when the value of D is greater than $D_{critical}$, the voltage v_2 waveform is rectangular shaped due to the continuous conduction mode of the currents through the transformer coils.

Thus, bearing in mind the waveform of Fig. 4 (d) which maximum value is $P_{1,max} = V_{npc} I_{1,max}$, one can determine the average power supply to the primary coil by calculating the area under a triangle multiplied by $(2/T)$, as follows:

$$P_1 = \left(\frac{L_2 V_{npc}^2 - M V_{npc} V_o}{L_1 L_2 - M^2}\right) D^2 T \tag{21}$$

Disregarding the losses in the PMSG and the interface rectifier and according to Fig. 2, the following energy balance equation can be written for the DC-link between the PMSG rectifier and the full-bridge inverter

$$\frac{C_{eq}}{2}\frac{dV_{npc}^2}{dt} = P_g - P_1 \tag{22}$$

where V_{npc} is the average value of the rectifier DC bus voltage, C_{eq} is the equivalent capacitance of the NPC rectifier, P_g is the power drained from the PMSG by the NPC rectifier and P_1 is the power supplied by the full-bridge inverter to the primary coil of the air-core transformer.

Substituting (21) into (22) and linearising the resulting expression around an equilibrium point allows one to write the following small-signal relation for $\widetilde{v}_{npc}$, in the frequency domain:

$$\widetilde{V}_{npc}(s) = \left[\frac{1}{\text{Den}(s)}\right]\widetilde{P}_g(s) + \left[\frac{\overline{D}^2 K_2 \overline{V}_{npc}}{\text{Den}(s)}\right]\widetilde{V}_o(s) - \\ - \left[\frac{2\overline{D}\left(K_1 \overline{V}_{npc} - K_2 \overline{V}_o\right)\overline{V}_{npc}}{\text{Den}(s)}\right]\widetilde{D}(s) \tag{23}$$

where $\text{Den}(s) = (sC_{eq}\overline{V}_{npc} + \overline{D}^2(2K_1\overline{V}_{npc} - K_2\overline{V}_o))$, $K_1 = (TL_2)/(L_1L_2 - M^2)$, $K_2 = (TM)/(L_1L_2 - M^2)$. The variables with the symbol (-) denote the steady-state operation point, while the symbol ($\widetilde{}$) is associated with the variables is used to represent small perturbations around the operating point.

Fig. 5 shows the block diagram relating the voltage $\widetilde{V}_{npc}(s)$ of the full-bridge inverter and the control signal $\widetilde{D}(s)$. The power supplied by the PMSG $\widetilde{P}_g(s)$ and the output voltage $\widetilde{V}_o(s)$ in (23) are disturbances, and for simplicity sake, are not represented in the diagram. The block $C_v(s)$ is the voltage controller, while the full-bridge inverter transfer function is represented by $G_{fb}(s) = \widetilde{V}_{npc}(s)/\widetilde{D}(s)$. The block with negative unit gain compensates for the reverse logic of the plant, since whenever the DC voltage is greater than the reference signal, the error $(\widetilde{V}_{npc}^* - \widetilde{V}_{npc})$ will be negative forcing the duty cycle D to decrease instead of increasing to transmit more energy to the HVDC link.

The controller $C_v(s)$ was designed as proportional-integral type to ensure a zero steady-state error for the DC bus voltage. Based on

block diagram of Fig. 5, it is possible to write the closed loop transfer function (24). The gains of the voltage controller can be calculated by comparing (24) with the canonical form of 2^{nd}–order transfer function yielding

$$k_{p,v} = \frac{2\xi C_{eq}\overline{V}_{npc}\omega_n - 2\overline{D}^2 K_1 \overline{V}_{npc} + \overline{D}^2 K_2 \overline{V}_o}{2\overline{D}\overline{V}_{npc}\left(K_1\overline{V}_{npc} - K_2\overline{V}_o\right)} \tag{25}$$

and,

$$k_{i,v} = \frac{C_{eq}\omega_n^2}{2\overline{D}\left(K_1\overline{V}_{npc} - K_2\overline{V}_o\right)} \tag{26}$$

where $k_{p,v}$ and $k_{i,v}$ are the proportional and integral gains of the voltage controller, respectively. The damping factor ξ and undamped natural frequency ω_n in (25) must be carefully chosen to ensure a fast response with limited overvoltage for the full-bridge DC capacitor.

III. The Design of The Air-Core Transformer

Bearing in mind the wind farm cluster shown in Fig. 9, it can be emphasized that the DC-DC SST must provide different insulation characteristics, depending on the position of the WEC unit in the cluster. The minimum isolation capacity is required in the units close to the grounding-point of the bipole, since the transformer windings must be equipped with insulation for the DC voltage of the interface rectifier. The first and last DC-DC SST units, on the other hand, require isolation capacity for the maximum and minimum HVDC link voltage, respectively. Challenges also exist when it comes to operating DC-DC SST units at high frequencies due to greater magnetic losses [20]. The DC-DC SST may also face problems related to asymmetric magnetization during variations in the HVDC link current.

The design of an air-core transformer would be an interesting alternative to avoid some of the problems mentioned above. The large dimensions of high-power wind-turbine towers make it possible to incorporate large coils in their interior. The cross-section view in Fig. 6 illustrates how an air-core transformer could be installed in a wind turbine tower. To facilitate the isolation, the secondary coil can be wound using an XLPE cable. Moreover, its cylindrical geometry does not impose any obstacle to accessing the nacelle by maintenance personnel.

As a downside, the low reluctance of the air-core makes the transformer to drain a high magnetization current from the source. Though, this unwanted effect can be minimized through a careful design of the transformer. A number of factors can positively affect such a characteristic, for instance, increasing the number of turns in the primary coil or the cross-sectional area of the coils or the frequency of the excitation source. Regarding the first and second options, they are limited by the height and diameter of the tower. Additionally, high frequencies can incur a considerable amount of skin and proximity-effect losses in the transformer winding wires. Besides, the operation frequency depends on the semiconductor devices switching capacity.

In the end, the optimum choice among the infinite possibilities that exist for constructive parameters and characteristics of the transformer is only possible by means of a properly tailored mathematical model that comprises all phenomena of interest. Once obtained, this model can be optimized under the consideration of a specific strategy, translated into an objective function. First such a model will be set forth.

In a first approach to the problem, windings capacitance, saturation and asymmetric magnetization will be ignored and the air-core transformer will be modeled simply by two magnetically coupled circuits. Due to the absence of a magnetic core, the air-core transformers generally have a higher leakage flux, resulting in a lower coupling factor k between the primary and secondary coils, which is mathematically described by (27), where L_1 and L_2 correspond to the self-inductances of the primary and secondary coils, respectively, and M represents the mutual inductance.

$$k = \frac{M}{\sqrt{L_1 L_2}} \tag{27}$$

The voltage gain is also highly affected by the higher leakage inductance. Disregarding the windings resistance and considering an hypothetical load $R_L = (V_o^2/P_o)$ connected across its output terminals, the voltage gain between primary and secondary coils is given by (28).

$$\frac{V_2}{V_1} = \sqrt{\frac{M^2 R_L^2}{\omega^2 M^4 - 2\omega^2 M^2 L_1 L_2 + \omega^2 L_1^2 L_2^2 + L_1^2 R_L^2}} \tag{28}$$

Now, an optimization problem that enables the search of a specific combination of inductance values for the transformer, at same time operational restrictions, such as no-load input current, voltage gain, voltage regulation, output power, among others, are satisfied is formulated in (29) and (30).

$$\underset{\mathbf{x}}{\text{minimize}}\ \mathbf{f}(\mathbf{x}) = L_1 + L_2 \tag{29}$$

$$\text{subject to } \Theta(\mathbf{x}) = \begin{cases} L_{1,min} \le L_1 \le L_{1,max} \\ L_{2,min} \le L_2 \le L_{2,max} \\ M_{min} \le M \le M_{max} \\ k_{min} \le k \le k_{max} \\ V_{2,min} \le V_2 \le V_{2,max} \\ P_2 \ge P_{2,min} \\ \gamma_a \le \frac{L_2}{L_1} \le \gamma_b \\ VR \le VR_{max} \\ I_{1,nl} \le \alpha I_{1,fl} \end{cases} \tag{30}$$

In the restrictions summarized in (30), $\mathbf{x} = [L_1, L_2, M]^\intercal$ corresponds to a vector containing a possible solution for the optimization problem; P_2 and V_2 are the power and voltage at the secondary coil, respectively; γ_a and γ_b are constants dependent on the number of turns per unit length of the primary and secondary coils, respectively.

The parameters γ_a and γ_b are important constraints in the optimization problem, since the transformer coils are wound with cables with different insulation layers [21]. The VR is the transformer voltage regulation calculated as given in (31), where $V_{2,nl}$ and $V_{2,fl}$ are the *RMS* secondary voltages at no-load and full-load, respectively.

$$VR = \left(\frac{V_{2,nl} - V_{2,fl}}{V_{2,fl}}\right) \times 100 \tag{31}$$

Moreover, the no-load current in the primary coil, $I_{1,nl}$ must also be limited to a certain fraction of the full-load current $I_{1,fl}$. This

$$\frac{\widetilde{V}_{npc}(s)}{\widetilde{V}^*_{npc}(s)} = \frac{2\left(\frac{\overline{D}\left(sk_{p,v}+k_{i,v}\right)\left(K_1\overline{V}_{npc}-K_2\overline{V}_o\right)}{C_{eq}}\right)}{s^2 + \left(\frac{\overline{D}^2\left(2K_1\overline{V}_{npc}-K_2\overline{V}_o\right)+2\overline{D}k_{p,v}\left(K_1\overline{V}_{npc}-K_2\overline{V}_o\right)\overline{V}_{npc}}{C_{eq}\overline{V}_{npc}}\right)s + \frac{2\overline{D}k_{i,v}\left(K_1\overline{V}^2_{npc}-K_2\overline{V}_{npc}\overline{V}_o\right)}{C_{eq}\overline{V}_{npc}}} \tag{24}$$

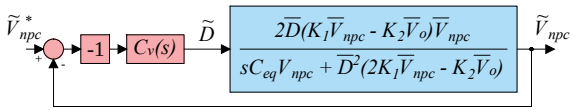

Fig. 5. Block diagram of the closed-loop control of the full-bridge DC voltage.

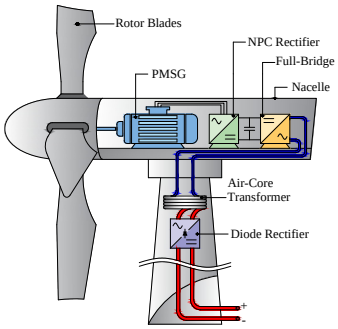

Fig. 6. Sectional view of the WEC tower and nacelle with the air-core transformer inside.

amount is modeled by means of the constant α, which is necessarily lower than unity and greater than zero. Assuming the cable resistance negligible, $I_{1,nl}$ can be approximated by (32).

$$I_{1,nl} = \frac{V_1}{\omega L_1} \tag{32}$$

Considering the parameters for the modular HVDC generator given in Table III and Table IV, the vector $\Theta(\mathbf{x})$ containing the constraints of the optimization problem was written as follows:

$$\Theta(\mathbf{x}) = \begin{bmatrix} 100\ \mu\text{H} \leq L_1 \leq 10\ \text{mH} \\ 100\ \mu\text{H} \leq L_2 \leq 20\ \text{mH} \\ 100\ \mu\text{H} \leq M \leq 10\ \text{mH} \\ 0.60 \leq k \leq 0.95 \\ 10\ \text{kV} \leq V_2 \leq 12.5\ \text{kV} \\ P_2 \geq 5\ \text{MW} \\ 1.25 \leq \frac{L_2}{L_1} \leq 2.25 \\ VR \leq 25\% \\ I_{1,nl} \leq 0.25 I_{1,fl} \end{bmatrix} \tag{33}$$

Assuming the above constraints, the solution of (29) using a mathematical software yields:

$$\mathbf{x} = \begin{bmatrix} L_1 \\ L_2 \\ M \end{bmatrix} = \begin{bmatrix} 5.517\ \text{mH} \\ 11.157\ \text{mH} \\ 7.453\ \text{mH} \end{bmatrix} \tag{34}$$

In order to design the transformer with inductances close to the ones listed in (34), the FEMM software was used [22]. For this purpose, the cylindrical arrangement with concentric coils was chosen aiming at an increased coupling factor. This geometry also facilitates the allocation of the coils inside the tower of WT, as shown in Fig. 6. Side and cross-section views of the transformer arrangement are shown in Fig. 7. The inductances obtained with FEMM analyses are given in Table I, for 1200 Hz of excitation frequency. The resistances of primary and secondary windings were calculated taking into account the skin and proximity effects.

Copper cables without shield layers for 15 kV and 220 kV with 500 mm^2 of cross section were respectively considered to wound the primary and secondary coils, which dimensions are given in Table II. The step-up transformer was constructed with 58 turns on the primary and 88 on the secondary. This configuration compensates the voltage drop across the leakage reactance and increases the voltage gain.

An external magnetic aluminium shield was used to attenuate the eddy current losses in the WT tower compartment. The aluminium

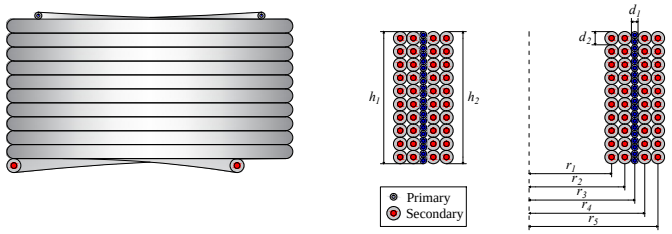

(a) (b)

Fig. 7. Air-core transformer coils arrangement: (a) side view and (b) cross-section view.

Table I
THE AIR-CORE TRANSFORMER PARAMETERS.

Parameter	Value
f	1200 Hz
R_1	218.838 mΩ
R_2	273.384 mΩ
L_1	6.070 mH
L_2	11.420 mH
M	7.703 mH
N_1:N_2	58:88

Table II
THE AIR-CORE COILS DIMENSIONS.

Parameter	Value	Parameter	Value
d_1	41.4 mm	r_2	1.416 m
d_2	111 mm	r_3	1.500 m
$h_1 = h_2$	2.443 m	r_4	1.584 m
r_1	1.305 m	r_5	1.695 m

shield was designed comprising six layers of 0.5 mm, resulting a 3 mm thickness aluminium jacket close to wind tower housing. In the project, a stretch of a steel wind tower was considered with 8 m of height, 5 m of inner diameter and 85 mm of thickness. Fig. 8 shows one quadrant ($r > 0$) of the axisymmetric model of the coils with the aluminium shield jacket simulated in FEMM. This result was obtained considering a secondary coil current of 500 A. Note that the distribution of magnetic field in wind tower housing is blocked by the aluminium shield, limiting the eddy losses to about 27 W. The coupling factor between the coils reached approximately 0.925, considering the inductance values from the FEMM simulations.

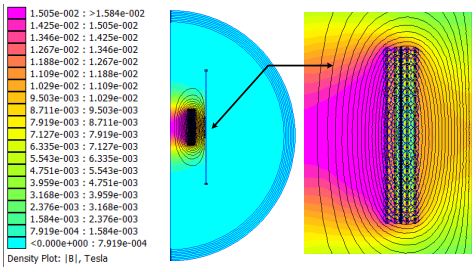

Fig. 8. Magnetic field distribution through the air-core transformer for 500 A on the secondary side. Finite element model simulation.

IV. Modelled System and Simulation Results

Fig. 9 shows the simplified diagram of the system modelled in PSCAD/EMTDC to investigate the performance of the DC-DC SST and its control strategy. The offshore wind cluster was implemented

by connecting sixty four 5 MW/10 kV WEC units in series to a VSC-HVDC transmission link. Table III shows the main parameters of each generating unit. In order to reduce the computational effort and simplify the digital simulation, each set of 16 WECs was grouped in a single block. The electrical parameters of the DC-DC solid-state transformer are give in Table IV.

Considering the data provided in [17], one can estimate the turbine $C_{p,max} = 0.434$ and $\lambda_{opt} = 11.6$ using and the mathematical model of the PSCAD/EMTDC. Then, from (8), it is possible to calculate the gain $k_{opt} = 1.044$ used by the OTC-MPPT algorithm.

The subsea cable was modelled in the PSCAD/EMTDC as a frequency-dependent phase model. The wind farm was considered placed 50 km away from the coast, and a 500 mm^2 XLPE cable of 320 kV/690 A was used to interconnect the offshore cluster to the onshore substation [23]. The onshore inverter is a 320 MW/640 kV modular multilevel converter, which controls the current through the DC link instead of its DC voltage. More details about the MMC control is given in [10]. In the last part of the diagram, the simulated system is connected to the mains through a 138/230 kV step-up transformer.

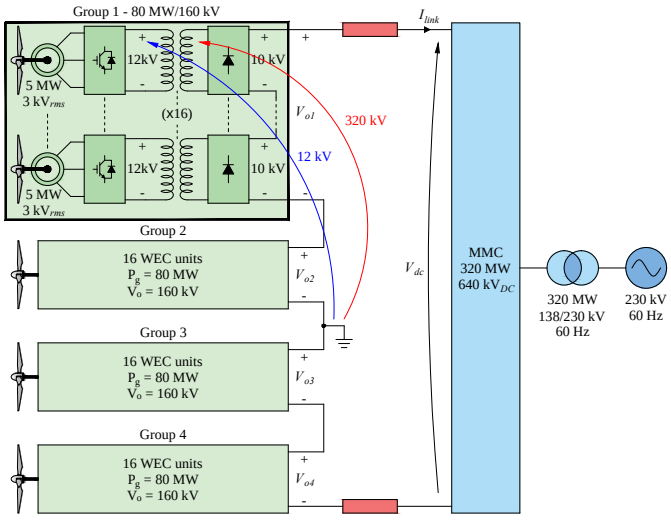

Fig. 9. Schematic diagram of the simulated system.

Table III
PARAMETERS OF THE PMSG AND NPC RECTIFIER.

Description	Symbol	Value
PMSG rated power	P_g	5 MW
PMSG line *rms* voltage	V_{Lg}	3 kV
PMSG frequency	f_g	60 Hz
PMSG equivalent resistance (stator + filter)	R_g	86 mΩ
PMSG equivalent inductance (stator + filter)	L_g	4.96 mH
NPC DC bus voltage	V_{npc}	12 kV
NPC rectifier switching frequency	f_{npc}	2.4 kHz
NPC rectifier capacitances	C_1, C_2	5000 µF

Table V shows the design parameters and the gains of the rectifier controllers. The gains were calculated using (6) and (10) in order to the PI controllers $C_{id}(s)$ and $C_{iq}(s)$ regulate the current drained from the PMSG and the resonant controller $C_{pr}(s)$ balances the DC capacitor voltages by compensating for the DC link midpoint current of the NPC rectifier. Table VI shows the design parameters and the gains of the voltage controller $C_v(s)$ of the DC-DC SST. This controller's gains were calculated by (25) and (26), according to the methodology presented in the first part of this work.

Table IV
PARAMETERS OF THE DC-DC SST.

Description	Symbol	Value
HVDC link current	I_{link}	450 A
Input DC voltage	V_{npc}	12 kV
Output DC voltage	V_o	10 kV
Output capacitance	C_o	400 µF
Full-bridge switching frequency	f_{sst}	1.2 kHz

Table V
NPC RECTIFIER CONTROLLERS GAINS.

Description	Symbol	Value
Current controller time constant	τ_{npc}	1.0 ms
Current controller proportional gain	$k_{p,npc}$	4.9549 V/A
Current controller integral gain	$k_{i,npc}$	86.0 V/(A s)
Resonant controller bandwidth	ω_b	7π rad/s
Resonant controller proportional gain	$k_{p,res}$	1.3524 V/A
Resonant controller resonant gain	$k_{r,res}$	23.3213 V/A

Table VI
DC-DC SST CONTROLLER GAINS.

Description	Symbol	Value
Undamped natural frequency	ω_n	30π rad/s
Damping ratio	ξ	0.9
Proportional gain	k_p	0.1122 $(\text{kV})^{-1}$
Integral gain	k_i	0.12679 $(\text{kV})^{-1}\text{s}^{-1}$

Two events will be investigated bellow. In $t = 0.1$ s, the reference voltage V^*_{npc} of the controllers of the first group will be increased in a step, from 11.5 kV to 12 kV, after that, in $t = 0.6$ s, the speed of wind arriving at the turbines of Group 1 will be decreased in a step, from rate speed (11.6 m/s) to 10.6 m/s. As previously explained, the same event is applied to all units in group. The WEC units of the other three groups in the cluster will continue supply rated powers and voltages.

Fig. 10(a) show the phase voltages of the NPC rectifier and the PMSG, both measured at phase "*a*" of the first WEC unit of Group 1. The slight asymmetry observed in the terminal voltage of the NPC rectifier is due to the action of the resonant controller balancing the voltages of the DC capacitors. Fig. 10(b) and Fig. 10(c) show the PMSG currents in *abc* and *dq* coordinates, respectively. These currents have a constant magnitude until $t = 0.6$ s. From this moment on, their amplitude decrease due to the reduction in power supplied by the WEC units of the first group. As a consequence of the modeling and control of the NPC rectifier in the synchronous coordinates, the reference signal for *d*–axis current is set to be zero, while the OTC algorithm generates the reference signal *q*–axis current in order to track the maximum power of the generator. Note that the frequencies of the PMSG and NPC phase voltages, as well as the three-phase currents, decrease with the reduction in wind speed. Fig. 10(d) shows the waveforms of the voltages of the NPC's capacitors. Note that these voltages are fully balanced by the resonant controller (10).

Fig. 11(a) and Fig. 11(b) show the input DC bus voltage and the reference signal of the controller, and the duty cycle of the first full-bridge inverter of the cluster, respectively. After the reference voltage changes, in $t = 0.1$ s, the DC-DC SST controller regulates the DC bus voltage very fast resulting in a small overshoot due to the damping factor ξ equals 0.9 (Table VI). In $t = 0.6$ s, the power supplied by the units of Group 1 decreases due to the reduction in wind speed. From that moment on, after a small dip in the DC bus voltage, the voltage controller reduced the duty-cycle D to force

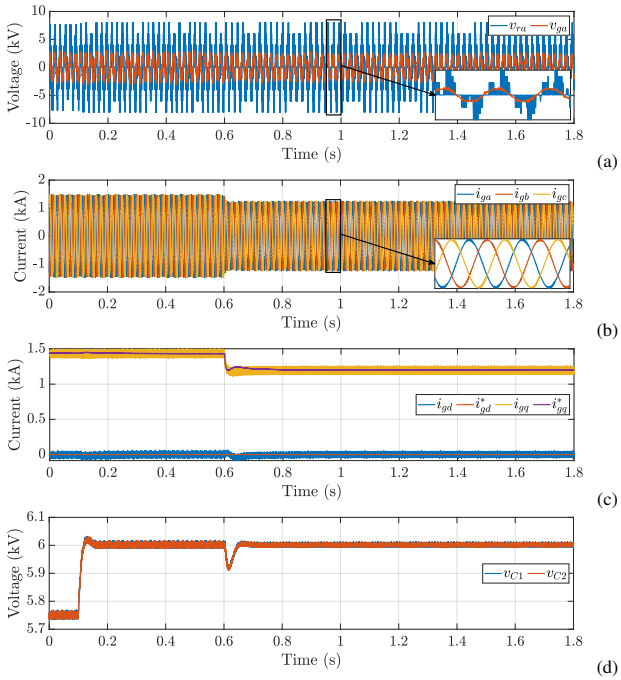

Fig. 10. First PMSG and NPC-rectifier unit waveforms: (a) phase *a* voltages of the NPC converter and generator, (b) three-phase currents of the generator, (c) *dq* currents of the generator and (d) NPC capacitors voltages.

the full-bridge inverter to transfer less power to the HVDC link. Fig. 11(b) also shows the dynamic behaviour of $D_{critical}$. As it depends directly of V_o and V_{npc}.

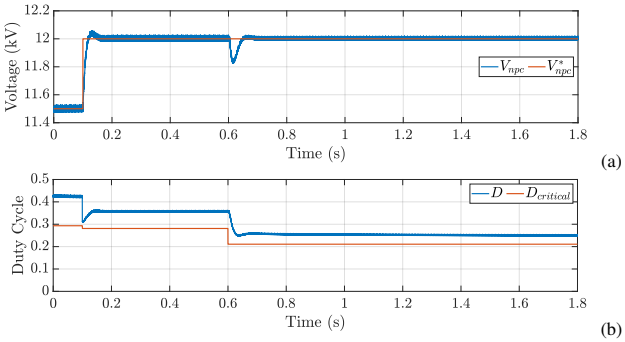

Fig. 11. DC-DC SST : (a) inner DC voltage and (b) the duty cycle for the first WEC unit.

Fig. 12(a) and Fig. 12(b) show the waveforms of the voltages and currents in the primary and secondary coils of the air-core transformer, respectively. After changing the value of the reference voltage V^*_{npc} in $t = 0.1$ s, the magnitude of the voltage on the primary coil is increased due to the change in the duty-cycle D. However, the magnitude of the voltage on the secondary coil does not vary as the amount of power supplied by the wind turbines, as well as the current through the DC link, does not change. The same behaviour is not observed for $t \geq 0.6$ s, when the reduction in power supplied by the wind turbines of the first group of WECs causes a decrease in the magnitude of the voltage in the secondary coil since less energy reaches the HVDC link. The details of the waveforms of the voltages and currents in the primary and secondary coils, with the exception of the moments of occurrence of the transient events, are very close to the theoretical waveforms discussed in the first part of this work.

Fig. 13(a) show the current through the HVDC link and its

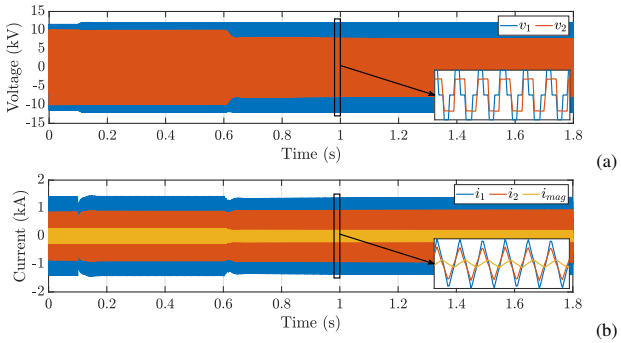

Fig. 12. Transformer: (a) voltages and (b) currents at the primary and secondary terminals and the magnetizing current.

reference signal. This current is controlled by the onshore inverter. Fig. 13(b) shows the output DC voltages of the four groups of WEC units. The variation of the reference voltages of the units of the first group in $t = 0.1$ s does not affect the ouput DC voltage of the four groups in the cluster since the amount of power supplied by all units is not changed. However, for $t \geq 0.6$ s, when the speed of the wind arriving the turbines of Group 1 decreases, the power supplied by these units reduces, decreasing the output DC voltage of this group. This change is seen as a disturbance by the DC-DC SST units of group 2 to 4, forcing a temporary increasing in their output voltages. Fig. 13(c) shows the onshore inverter DC bus voltage. The behaviour of this voltage is consequence of what occurs with the WEC output voltages. For the reference change, it increase in the instant of the disturb, and come back to the previous value after this. For the wind speed variation, the DC link voltage decrease, because the power injected into the DC link also decreases.

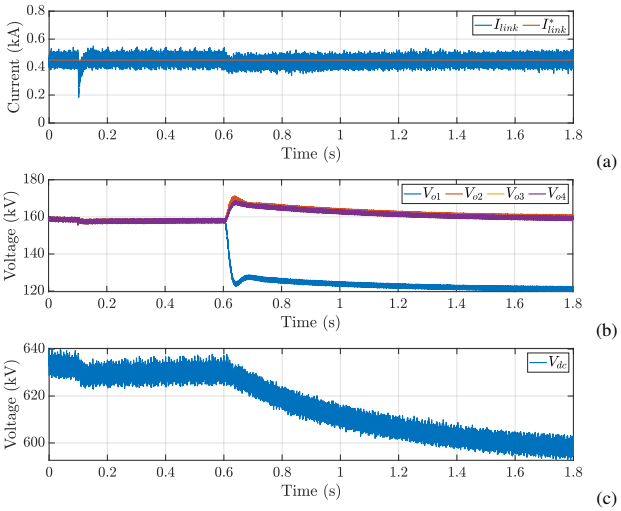

Fig. 13. HVDC link waveforms: (a) DC link current, (b) output DC voltages of the groups of WECs and (c) DC voltage of the onshore inverter.

V. Conclusions

This work presented the design and control steps of a DC-DC solid-state transformer used to connect the wind turbines of an offshore farm in series with a DC transmission link. This layout has the advantage of does not require a bulky power transformer to step-up the offshore network voltage to the transmission level, or a large rectifier station to convert the generated electricity to DC. The galvanic isolation between the WEC components and the DC

link is ensured by air-core transformer. Mathematical models were developed for the PMSG, the NPC rectifier and the DC-DC SST. These models were used to derive transfer functions and to design the controllers used to regulate the transfer of energy from the PMSG to the HVDC link. Although the PMSG frequency depends on the wind speed, the DC-DC SST voltages and currents are not affected, since the control systems of the three-phase rectifier and of the full-bridge inverter are independent. On the other side of the HVDC link, a modular multilevel converter injects the energy from the wind farm into the electrical network. PSCAD/EMTDC simulation results were used to demonstrate the effectiveness of the solid-state transformer to isolate the PMSG and NPC-rectifiers from the HVDC link, in steady-state and dynamic operation, when variations in the reference voltage of the DC-DC SST and the reduction of the power supplied by wind turbines were simulated. Furthermore, the simulations made it possible to evaluate the voltages and currents at different points in the modelled system, from the PMSG to the subsea DC cables.

ACKNOWLEDGMENTS

The authors would like to express their gratitude for the support received from the Federal University of Juiz de Fora and the Federal Centre of Technological Education of Minas Gerais. This study was also financed in part by the PETROBRAS Company (Cooperation Contract: 5850.0103831.17.9) and the National Council for Scientific and Technological Development (CNPq).

REFERENCES

[1] O. Anaya-Lara, D. Campos-Gaona, E. Moreno-Goytia, and G. Adam, Offshore wind energy generation. John Wiley & Sons, 2014.

[2] V. Yaramasu, B. Wu, P. C. Sen, S. Kouro, and M. Narimani, "High-power wind energy conversion systems: State-of-the-art and emerging technologies," Proceedings of the IEEE, vol. 103, no. 5, pp. 740–788, 2015.

[3] G. Quinonez-Varela, G. Ault, O. Anaya-Lara, and J. McDonald, "Electrical collector system options for large offshore wind farms," IET Renewable Power Generation, vol. 1, no. 2, pp. 107–114, 2007.

[4] M. Liserre, R. Cardenas, M. Molinas, and J. Rodriguez, "Overview of multi-MW wind turbines and wind parks," IEEE Transactions on Industrial Electronics, vol. 58, no. 4, pp. 1081–1095, 2011.

[5] S. Lundberg, "Evaluation of wind farm layouts," EPE journal, vol. 16, no. 1, pp. 14–21, 2006.

[6] R. Ryndzionek and Ł. Sienkiewicz, "Evolution of the HVDC link connecting offshore wind farms to onshore power systems," Energies, vol. 13, no. 8, p. 1914, 2020.

[7] P. M. Meshram and V. B. Borghate, "A simplified nearest level control (nlc) voltage balancing method for modular multilevel converter (mmc)," IEEE Transactions on Power Electronics, vol. 30, no. 1, pp. 450–462, 2014.

[8] Staff, EEMIT, Magnetic Circuits and Transformers: A First Course for Power and Communication Engineers. MIT Press, USA, 1946.

[9] E. Veilleux and P. W. Lehn, "Interconnection of direct-drive wind turbines using a series-connected dc grid," IEEE Transactions on Sustainable Energy, vol. 5, no. 1, pp. 139–147, 2014.

[10] A. O. Almeida, M. A. Tomim, P. M. Almeida, and P. G. Barbosa, "A control strategy for an offshore wind farm with the generating units connected in series with a vsc-hvdc transmission link," Electric Power Systems Research, vol. 180, pp. 106–121, 2020.

[11] S. Lundberg, "Wind farm configuration and energy efficiency studies," Ph.D. dissertation, Chalmers University of Technology, Sweden, 2006.

[12] G. Shi, J. Zhang, X. Cai, M. Zhu, and L. Yao, "Improved variable speed control of series-connected dc wind turbines for offshore wind power collection to high-voltage direct current system," IET Renewable Power Generation, vol. 10, no. 6, pp. 843–851, 2016.

[13] H. Zhang, F. Gruson, D. M. F. Rodriguez, and C. Saudemont, "Overvoltage limitation method of an offshore wind farm with dc series-parallel collection grid," IEEE Transactions on Sustainable Energy, vol. 10, no. 1, pp. 204–213, 2019.

[14] M. Guan, "A series-connected offshore wind farm based on modular dual-active-bridge (dab) isolated dc-dc converter," IEEE Transactions on Energy Conversion, vol. 34, no. 3, pp. 1422–1431, 2019.

[15] B. Wu, Y. Lang, N. Zargari, and S. Kouro, Power conversion and control of wind energy systems. John Wiley & Sons, 2011, vol. 76.

[16] A. Yazdani and R. Iravani, Voltage-sourced converters in power systems. John Wiley & Sons, 2010.

[17] V. Yaramasu, B. Wu, M. Rivera, and J. Rodriguez, "A new power conversion system for megawatt pmsg wind turbines using four-level converters and a simple control scheme based on two-step model predictive strategy—part ii: Simulation and experimental analysis," IEEE Journal of Emerging and Selected Topics in Power Electronics, vol. 2, no. 1, pp. 14–25, 2014.

[18] Y. Zhang, J. Li, X. Li, Y. Cao, M. Sumner, and C. Xia, "A method for the suppression of fluctuations in the neutral-point potential of a three-level npc inverter with a capacitor-voltage loop," IEEE Transactions on Power Electronics, vol. 32, no. 1, pp. 825–836, 2017.

[19] C. Xia, F. Zhou, Z. Wang, and X. He, "Equivalent switch circuit model and proportional resonant control for triple line-voltage cascaded voltage-source converter," IEEE Transactions on Power Electron, vol. 28, no. 5, pp. 2389–2401, 2013.

[20] C. W. T. McLyman, Transformer and inductor design handbook. CRC press, 2016.

[21] H. Nagaoka, "The inductance coefficients of solenoids," Journal of the College of Science, vol. 27, no. 3, p. 31, 1909.

[22] D. Meeker. (2015) Finite element method magnetics: User's manual (version 4.2). FEMM. Accessed: 2020-01-30. [Online]. Available: https://www.femm.info/wiki/HomePage

[23] ABB. (2010) XLPE submarine cable system: User's guide. Accessed: 2019-01-01. [Online]. Available: https://new.abb.com/docs/default-source/ewea-doc/xlpe-submarine-cable-systems-2gm5007.pdf